

# Detection of a transit of the super-Earth 55 Cnc e with *Warm Spitzer*<sup>★</sup>

B.-O. Demory<sup>1</sup>, M. Gillon<sup>2</sup>, D. Deming<sup>3</sup>, D. Valencia<sup>1</sup>, S. Seager<sup>1</sup>, B. Benneke<sup>1</sup>, C. Lovis<sup>4</sup>, P. Cubillos<sup>5</sup>, J. Harrington<sup>5</sup>, K. B. Stevenson<sup>5</sup>, M. Mayor<sup>4</sup>, F. Pepe<sup>4</sup>, D. Queloz<sup>4</sup>, D. Segransan<sup>4</sup>, S. Udry<sup>4</sup>

<sup>1</sup> Department of Earth, Atmospheric and Planetary Sciences, Department of Physics, Massachusetts Institute of Technology, 77 Massachusetts Ave., Cambridge, MA 02139, USA

<sup>2</sup> Institut d'Astrophysique et de Géophysique, Université de Liège, Allée du 6 Août 17, Bat. B5C, 4000 Liège, Belgium

<sup>3</sup> Department of Astronomy, University of Maryland, College Park, MD 20742-2421, USA

<sup>4</sup> Observatoire de Genève, Université de Genève, 51 Chemin des Maillettes, 1290 Sauverny, Switzerland

<sup>5</sup> Planetary Science Group, Department of Physics, University of Central Florida, Orlando, FL 32816-2385, USA

Received date / accepted date

## ABSTRACT

We report on the detection of a transit of the super-Earth 55 Cnc e with *Warm Spitzer* in IRAC's 4.5 $\mu$ m band. Our MCMC analysis includes an extensive modeling of the systematic effects affecting *Warm Spitzer* photometry, and yields a transit depth of  $450 \pm 50$  ppm, which translates to a planetary radius of  $2.13^{+0.14}_{-0.13} R_{\oplus}$  as measured in IRAC 4.5 $\mu$ m channel. A planetary mass of  $7.98 \pm 0.69 M_{\oplus}$  is derived from an extensive set of radial-velocity data, yielding a planetary density of  $0.83 \pm 0.18 \rho_{\oplus}$ . Interestingly, the derived radius is  $1.3\times$  larger than the one recently reported in the visible by Winn et al. Thanks to the brightness of its host star ( $V = 6$ ,  $K = 4$ ), 55 Cnc e is a unique target for the thorough characterization of a super-Earth orbiting around a solar-type star.

**Key words.** binaries: eclipsing – planetary systems – stars: individual: 55 Cnc - techniques: photometric

## 1. Introduction

Radial velocity (RV), microlensing and transit surveys have revealed the existence in our Galaxy of a large population of planets with a mass of a few to  $\sim 20$  Earth masses (Lovis et al. 2009; Sumi et al. 2010; Borucki et al. 2011). Based on their mass (or minimum mass for RV planets), these planets are loosely classified as “super-Earths” ( $M_p \leq 10 M_{\oplus}$ ) and “Neptunes” ( $M_p > 10 M_{\oplus}$ ). This classification is based on the theoretical limit for gravitational capture of H/He,  $\sim 10 M_{\oplus}$  (e.g., Rafikov 2006), and thus implicitly assumes that Neptunes are predominantly ice giants with a significant H/He envelope, and that most super-Earths are massive terrestrial planets. Still, the diversity of this planetary population is probably much larger than sketched by this simple division, as we can expect from the stochastic nature of planetary formation.

The first transit of one of these low-mass planets, GJ 436 b, was detected in 2007 (Gillon et al. 2007). Thanks to its transiting nature, the actual mass ( $M_p = 23.2 \pm 0.8 M_{\oplus}$ ) and radius ( $R_p = 4.22 \pm 0.10 R_{\oplus}$ ) of GJ 436 b could be accurately determined (Torres, 2007), indicating for this “hot Neptune” a mass, radius and density indeed very similar to the ice giant planets Uranus and Neptune. More recently, several other transiting low-mass planets were de-

tected. While many more planet candidates detected by the *Kepler* mission are waiting for confirmation (Borucki et al. 2011), the first confirmed low-mass transiting planets already show a large diversity. Some of these planets, like HAT-P-11b (Bakos et al. 2010) and Kepler-4b (Borucki et al. 2010b), are similar to Neptune and GJ 436 b. Kepler-11c (Lissauer et al. 2011) seems to be a smaller version of Neptune, while HAT-P-26 b (Hartman et al. 2010) has a much lower density ( $0.4 \pm 0.10 \text{ g cm}^{-3}$  vs  $1.64 \text{ g cm}^{-3}$  for Neptune) that is consistent with a significantly larger H/He fraction. The super-Earths CoRoT-7 b (Léger et al. 2009, Hatzes et al. 2010) and Kepler-10b (Batalha et al. 2011) are probably massive rocky planets formed in the inner part of their protoplanetary disks. The super-Earth, GJ 1214 b (Charbonneau et al. 2009) is still mysterious in nature. Its large radius ( $R_p = 2.44 \pm 0.21 R_{\oplus}$ , Carter et al. 2011) suggests a significant gaseous envelope that could originate from the outgassing of the rocky/icy surface material of a terrestrial planet or that could be of primordial origin, making it a kind of “mini-Neptune” (Rogers & Seager 2010). Recent transit transmission spectrophotometric measurements for GJ 1214 b seem to rule out a cloud-free atmosphere composed primarily of hydrogen (Bean et al. 2010, Désert et al. 2011), but more atmospheric measurements are needed to determine the exact nature of its envelope. The case of GJ 1214 b shows nicely that understanding the true nature of a low-mass exoplanet could require not only precise measurements of its mass and radius, but also a study of its atmospheric properties.

Send offprint requests to: demory@mit.edu

<sup>★</sup> The photometric time series used in this work are available in electronic form at the CDS via anonymous ftp to cdsarc.u-strasbg.fr (130.79.128.5) or via http://cdsweb.u-strasbg.fr/cgi-bin/qcat?J/A+A/

Among all the low-mass transiting exoplanets detected so far, only GJ 1214 b and GJ 436 b, and to a lesser extent HAT-P-11 b and HAT-P-26 b, orbit around stars small enough and bright enough in the infrared to make possible a thorough atmospheric characterization with existing or future facilities like JWST (e.g., Shabram et al. 2011). Improving our understanding of the low-mass planet population orbiting around solar-type stars requires that such planets are detected in transit in front of much nearer/brighter host stars than the targets of surveys like CoRoT (Barge et al. 2008) or *Kepler* (Borucki et al. 2010a). This is the main goal of two ambitious space mission projects in development: PLATO (Catala et al. 2010) and TESS (Ricker et al. 2010). Still, another and more straightforward possibility exists. Doppler surveys target bright nearby stars, and they have now detected enough nearby low-mass planets to make highly probable that a few of them transit their parent stars. This motivated us to search with *Spitzer* for transits of low-mass Doppler planets having the highest transit probability. In a previous paper (Gillon et al. 2010, hereafter G10), we described the reasons that have led us to conclude that *Spitzer* and its Infra-Red Array Camera (IRAC, Fazio et al. 2004) were the best instrumental choice for this transit search, and presented the results of our *Spitzer* cycle 5 program targeting HD 40307 b (Mayor et al. 2009). The rest of our program consist of a cycle 6 DDT program (ID 60027) of 100 hours that targeted ten other low-mass planets. *Spitzer*'s cryogen was depleted at the end of cycle 5, and these observations were thus carried out in non-cryogenic mode ("*Warm Spitzer*").

The recent announcement of 55 Cnc e transits detection by the *MOST* satellite (Winn et al. 2011) motivated the publication of this paper. Our initial analysis of the *Warm Spitzer* data taken in last January concluded to a transit detection but also that several sources of instrumental effects needed to be fully characterized before securing the detection. We only recently obtained a satisfactory instrumental model for *Warm Spitzer* photometry, through a global analysis of calibration data and of all the observations of our cycle 6 program (Gillon et al., in prep.). Once applied to our 55 Cnc data, this instrumental model leads not only to the firm detection of the transit of 55 Cnc e, but also to a precise determination of its transit parameters.

Section 2 presents our derivation of the transit ephemeris from the published RVs. In Section 3, we present our data and their analysis that reveals the transiting nature of the planet. We discuss our transit detection and its implications in Section 4.

## 2. Transit ephemeris estimation

We performed a global analysis of all the available RVs for 55 Cnc to estimate the most reliable transit ephemeris for 55 Cnc e. This analysis was done with the adaptative Markov Chain Monte-Carlo (MCMC) algorithm described in G10. We assumed Keplerian orbits for the five planets orbiting 55 Cnc, after having checked that planet-planet interactions had negligible influence on our solutions, using for this purpose the *Systemic Console* software package (Meschiari et al. 2009). Our analysis was based on the orbital solution recently presented for 55 Cnc e by Dawson & Fabrycky (2010). As shown by these authors, the orbital period value initially reported for this planet, 2.8 days (McArthur et al. 2004; Fischer et al. 2008), was an alias of the true period,

0.74 day. We verified this result by making two independent MCMC analysis of the RVs, one assuming  $P \sim 0.74$  day and the other assuming  $P \sim 2.8$  days. Using the Bayesian Information Criterion (BIC; e.g. Carlin & Louis 2008) to deduce the relative marginal likelihood of both models from the MCMC outputs, and assuming that these models have the same prior probability, we obtained a Bayes factor of  $\sim 10^{16}$  in favor of the  $P = 0.74$  day model, indicating a decisive strength of evidence for this model (Jeffreys 1961).

In addition to some basic parameters for the host star, the origin of the RVs used as input data, and a description of our *Warm Spitzer* observations, Table 1 provides the most relevant results of our MCMC analysis for 55 Cnc e. The large transit probability,  $\sim 28\%$ , and the very well constrained transit ephemeris ( $1\sigma$  error  $< 1$  hour in 2011) of this super-Earth ( $M_p = 8.0 \pm 0.7 M_\oplus$ ) made it an extremely interesting target for our transit search program.

## 3. Data description, analysis and results

55 Cnc was observed by *Spitzer* on 06 January 2011 from 09h41 to 14h39 UT. The data consist of 5240 sets of 64 individual subarray images obtained by the IRAC detector at  $4.5 \mu\text{m}$  with an integration time of 0.01s, and calibrated by the *Spitzer* pipeline version S18.18.0. They are available on the *Spitzer* Heritage Archive database<sup>1</sup> under the form of 5240 Basic Calibrated Data (BCD) files. We first converted fluxes from the *Spitzer* units of specific intensity (MJy/sr) to photon counts, then performed aperture photometry on each subarray image with the IRAF/DAOPHOT<sup>2</sup> software (Stetson, 1987). We tested different aperture radius and background annuli, the best result being obtained with an aperture radius of 3 pixels and a background annulus extending from 11 to 15.5 pixels from the PSF center. The center of the PSF was measured by fitting a Gaussian profile to each image. We discarded the first ten minutes of data to allow the detector to stabilize. The  $x$ - $y$  distribution of the measurements was then looked at, and we discarded the few measurements having a very different position than the bulk of the data. For each block of 64 subarray images, we then discarded measurements with discrepant values of flux, background,  $x$  and  $y$  positions using a  $\sigma$  median clipping ( $5\sigma$  for the flux and  $10\sigma$  for the other parameters), and the resulting values were averaged, the photometric error being taken as the error on the average flux measurement. At this stage, a  $50\sigma$  slipping median clipping was used on the resulting light curve to discard totally discrepant fluxes.

Fig. 1 shows the resulting raw light curve, and the time-series for the background and the  $x$  and  $y$  positions. As can be seen in Fig. 1 and Fig. 2, the measured background showed an unusual evolution during the run. It remained stable during  $\sim 3.5$  hrs, then it increased abruptly of a few %, and finally its scatter increased largely. Such a behavior is most probably of instrumental origin. We observed it for several other targets of our *Warm Spitzer* program (Gillon et al., in prep.), and in all cases it was correlated to a sharp increase of the effective gain of the detector, suggesting an electronic or thermal instability of the detector.

<sup>1</sup> <http://sha.ipac.caltech.edu/applications/Spitzer/SHA>

<sup>2</sup> IRAF is distributed by the National Optical Astronomy Observatory, which is operated by the Association of Universities for Research in Astronomy, Inc., under cooperative agreement with the National Science Foundation.

Star	55 Cnc
Distance $d$ [parsec]	$12.34 \pm 0.12^1$
$V$ magnitude	$5.96 \pm 0.01^2$
$K$ magnitude	$4.02 \pm 0.03^3$
Spectral type	K0V - G8V <sup>4</sup>
Effective temperature $T_{\text{eff}}$ [K]	$5234 \pm 30^5$
Surface gravity $\log g$	$4.45 \pm 0.08^5$
Metallicity Fe/H [dex]	$+0.31 \pm 0.04^5$
Mass $M_*$ [ $M_{\odot}$ ]	$0.94 \pm 0.05^4$
Radius $R_*$ [ $R_{\odot}$ ] <sup>a</sup>	$0.95 \pm 0.02$
RV data	
	250 Lick <sup>4</sup>
	70 Keck <sup>4</sup>
	119 HET <sup>6</sup>
	48 ELODIE <sup>7</sup>
Planet (MCMC results)	55 Cnc e
Minimal Mass $M_p \sin i$ [ $M_{\oplus}$ ]	$7.98 \pm 0.69$
Expected Radius $R_p$ [ $R_{\oplus}$ ] <sup>b</sup>	1.3 - 5.7
Expected Area ratio $(R_p/R_*)^2$ [ppm]	150 - 3000
Equilibrium temperature $T_{\text{eq}}$ [K] <sup>c</sup>	$1967 \pm 30$
$T_{\text{transit}} - 2450000$ [HJD]	$5568.005 \pm 0.026$
$T_{\text{occultation}} - 2450000$ [HJD]	$5568.364 \pm 0.028$
Orbital period $P$ [d]	$0.7365430 \pm 0.0000059$
Central transit duration $W_{b=0}$ [min]	$98 \pm 2$
RV semi-amplitude $K$ [ $\text{km s}^{-1}$ ]	$5.92 \pm 0.45$
Semi-major axis $a$ [AU]	$0.01564 \pm 0.00028$
Eccentricity $e$	$0.057^{+0.064}_{-0.041}$
Argument of periastron $\omega$ [deg]	$170^{+90}_{-130}$
Prior transit probability [%]	$27.9 \pm 1.7$
Prior occultation probability [%]	$28.2 \pm 1.8$
<i>Warm Spitzer</i> data	
Channel [ $\mu\text{m}$ ]	4.5
AOR <sup>d</sup>	39524608
Exposure time [s]	0.01
$N_{\text{BCD}}$ <sup>e</sup>	5240
Duration [hr]	5

**Table 1.** Basic data for the star 55 Cnc, relevant results of our MCMC analysis for 55 Cnc e, and description of the data (RVs + *Warm Spitzer* observations) used in this work. <sup>1</sup>Van Leeuwen (2007). <sup>2</sup>Turon et al. (1993). <sup>3</sup>Skrutskie et al. (2006). <sup>4</sup>Fischer et al. (2008). <sup>5</sup>Valenti & Fischer (2005). <sup>6</sup>Mac Arthur et al. (2004). <sup>7</sup>Naef et al. (2004). <sup>a</sup>From  $V$  magnitude,  $T_{\text{eff}}$  and Hipparcos parallax, taking bolometric correction from Flower (1996). <sup>b</sup>Assuming  $M_p \sin i = M_p$ . The minimum and maximum values correspond, respectively, to a pure iron and a pure hydrogen planet (Seager et al. 2007). <sup>c</sup>Assuming a null albedo and a heat distribution factor  $f' = 1/4$  (Seager 2010). <sup>d</sup>AOR = Astronomical Observation Request = *Spitzer* observing sequence. <sup>e</sup>BCD = Basic Calibrated Data = block of 64 subarray exposures.

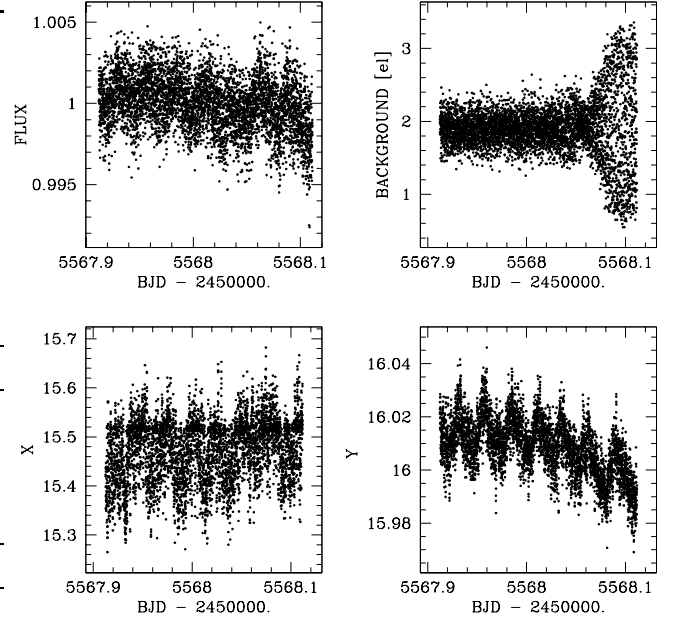


**Fig. 1.** *Top left:* raw light curve obtained for 55 Cnc. *Top right:* background time-series for this run. *Bottom:* time-series for the  $x$  (left) and  $y$  (right) positions of the stellar center.

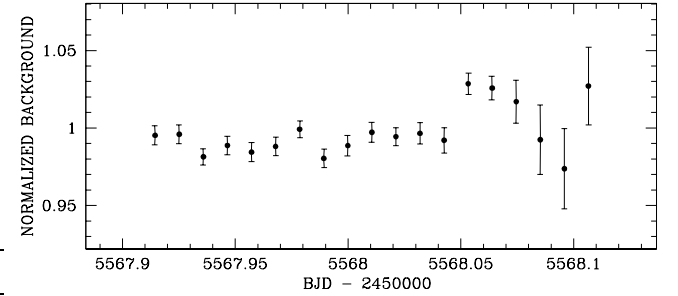


**Fig. 2.** Background time-series for the 55 Cnc data, after normalization and binning per 15 minutes intervals.

We included this instrumental effect in our data modeling (see below).

The IRAC 3.6 and 4.5  $\mu\text{m}$  detectors are composed of InSb arrays that show a strong intrapixel quantum efficiency (QE) variability, the QE being maximal in the middle of the pixel and decreasing towards the edges. The full-width at half maximum (FWHM) of the point-spread function (PSF) is  $\sim 1.7$  pixels. This undersampling of the PSF combined with the QE intrapixel variability leads to a strong dependence of the measured stellar flux on the exact location of the PSF center in a pixel. As *Spitzer*'s pointing wobbles with an amplitude of  $\sim 0.1$  pixel and a period of  $\sim 1$ h, this leads to a severe systematic effect in the photometric time-series acquired at 3.6 and 4.5  $\mu\text{m}$ , known as the “pixel-phase” effect. This effect was already present in the cryogenic part of the *Spitzer* mission and is very-well documented (e.g. Knutson et al. 2008 and references therein). It is the main limit to the photometric precision of *Warm Spitzer* (e.g. Ballard et al. 2010). From a comprehensive

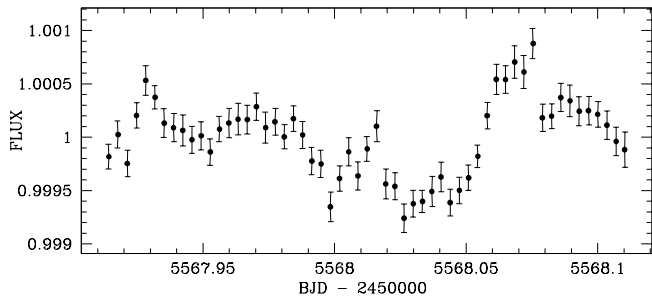


**Fig. 3.** 55 Cnc light curve corrected for the “pixel-phase” effect using a  $2^{nd}$  order position polynomial and binned to intervals of 5 min.

analysis, the *Spitzer* engineering team identified recently the cause of the *Spitzer* pointing wobble as the thermal cycling of a heater used to keep a battery within its nominal temperature range<sup>3</sup>. After extensive testing and review, it was decided to reduce by a factor two the thermal amplitude of the cycling while increasing its frequency to make it differ more from the typical frequency of planetary transits and occultations. Our data were obtained after this heater change. The correlation between the measured fluxes and the stellar image position is clearly noticeable in the raw light curve, the resulting periodic pattern having a typical period  $\sim 35$  min, corresponding to a cycle of the heater after the engineering change. We modeled this “pixel-phase” effect with the following  $2^{nd}$ -order  $x$  and  $y$  position polynomial:

$$A(dx, dy) = a_1 + a_2 dx + a_3 dx^2 + a_4 dy + a_5 dy^2 + a_6 dx dy, \quad (1)$$

where  $dx$  and  $dy$  are the distance of the PSF center to the center of the pixel. This model for the “pixel-phase” effect is quite classical in the exoplanet literature (e.g. Knutson et al. 2008, Désert et al. 2009). Correcting the light curve with the best-fit “pixel-phase” model lead to the light curve visible in Fig. 3. It shows a drop of brightness with an amplitude compatible with a transit of 55 Cnc e. It also shows some other low-amplitude flux modulations that are caused by other *Warm Spitzer* systematic effects (see below).

One could argue that the transit-like pattern could be caused by the imperfect correction of the “pixel-phase” effect by the function shown in Eq. 1. This is very unlikely, as the duration of the transit-like structure does not correspond to the one of the wobbles of the stellar position on the chip. To discard firmly this possibility, we tried  $3^{rd}$  and  $4^{th}$ -order version of Eq. 1 that led to very similar light curves. We also corrected the “pixel-phase” effect by a totally different method that relies only on the data themselves and not on any numerical function. We divided the pixel area sampled by the PSF center into  $33 \times 33$  small boxes. If at least 5 subarray measurements fell into a given box, and if these measurements sampled at least 0.14 days (70% of the duration of the run) the corresponding measurements were divided by their mean value. If these two conditions were not met for a given box, its measurements were discarded.

The reduction procedure was then identical to the one described above. The light curve obtained after this correction by an “intrapixel flatfield” was totally similar (pattern, scatter) to the one visible in Fig. 3. To assess the dependency of the observed transit-like structure on the details of the reduction procedure several independent reductions of the data were performed by four of us (M. G., B.-O. D., D. D., P. C.), all using different reduction and detrending procedures. We also tested performing photometry on the 5240 images resulting from the averaging of the 64 subarray images of each BCD file, using a median filter to reject outlying pixels. Finally, we inspected the light curves obtained without background subtraction. In all cases, the obtained light curves were very similar to the one shown in Fig. 3, confirming the independence of the obtained photometry on the details of the reduction procedure.

At this stage, we performed a thorough MCMC analysis of our photometry to deduce the transit detection significance, using as input data the raw light curve obtained with an aperture of 3 pixels. Our model assumed a mass of  $0.94 \pm 0.05 M_{\odot}$  for 55 Cnc (Valenti & Fischer 2005), and a circular orbit with  $P = 0.736543$  days for 55 Cnc e. We used the model of Mandel & Agol (2002) for the transit, in addition to the following model for the photometric variations of instrumental and stellar origin:

$$A(dx, dy, dt) = a_1 + a_2 dx + a_3 dx^2 + a_4 dy + a_5 dy^2 + a_6 dx dy + a_7 dt + a_8 dt^2 + a_9 \sin\left(\frac{dt - a_{10}}{a_{11}}\right) + a_{12} \log dt + a_{13} \log dt^2, \quad (2)$$

where  $dt$  is the time elapsed since 2455568.05 BJD, i.e. the time at which the background increases sharply (Fig. 1 & 2). The  $a_{12}$  and  $a_{13}$  terms were only applied for  $dt > 0$ . The six first terms of this equation correspond to the “pixel-phase” model (Eq. 1). The purpose of the linear and quadratic terms in  $dt$  is to model a possible smooth variation of the stellar brightness. The other terms result from our extensive analysis of our entire set of *Warm Spitzer* data (Gillon et al., in prep.) and of available calibration data that lead us to conclude to a low-amplitude periodic variability of the effective gain of the detector, its typical period lying between 30 and 60 minutes and its amplitude being of only a few dozens of ppm. Considering the challenging photometric precision required by our program, it is very important to take it into account, justifying the sinus term in Eq. 2. We also know from our experience with *Warm Spitzer* data that a “background explosion” such as the one affecting the last part of our data is correlated to a sharp increase of the effective gain of the detector that is very well modeled by the last two terms of Eq. 2.

The following parameters were jump parameters<sup>4</sup> in our analysis: the planet/star area ratio  $(R_p/R_*)^2$ , the transit width (from first to last contact)  $W$ , the impact parameter  $b = a \cos i/R_*$ , and the time of minimum light  $T_0$ . We assumed a uniform prior distribution for these jump parameters, but we imposed a Gaussian prior for the stellar radius  $R_*$  based on  $R_* = 0.95 \pm 0.03 R_{\odot}$  (Table 1). We assumed a quadratic limb-darkening law with coefficients  $u_1 = 0.0706$  and  $u_2 = 0.1471$ . These values were drawn

<sup>3</sup> <http://ssc.spitzer.caltech.edu/warmmission/news/21oct2010memo.pdf>

<sup>4</sup> Jump parameters are the parameters that are randomly perturbed at each step of the MCMC.

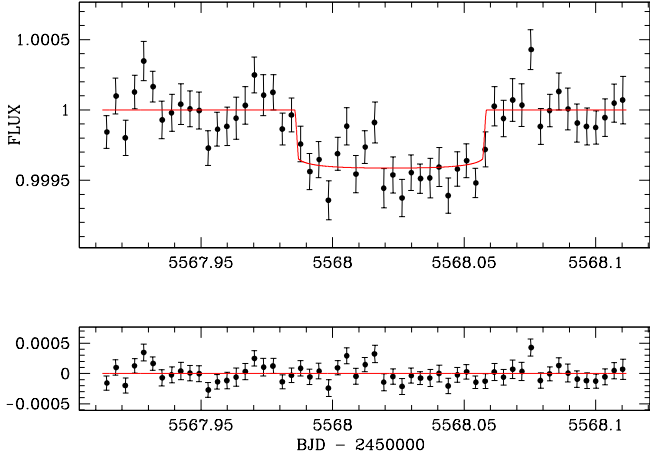


**Fig. 4.** *Top:* 55 Cnc light curve divided by the best-fit baseline model, binned to intervals of 5 min, with the best-fit transit model overimposed. *Bottom:* residuals of the fit binned to intervals of 5 min.

from the theoretical tables of Claret & Bloemen (2011) for the IRAC 4.5  $\mu\text{m}$  bandpass and for  $T_{\text{eff}} = 5250$  K,  $\log g = 4.5$  and  $[\text{Fe}/\text{H}] = +0.3$ . The 13 coefficients of the baseline models (Eq. 2) were determined by least-square minimization at each steps of the Markov chains (see G10 and references therein for details). The correlated noise present in the LC was taken into account as described by G10, i.e., a scaling factor  $\beta_r$  was determined from the standard deviation of the binned and unbinned residuals of a preliminary MCMC analysis, and it was applied to the error bars. Several binning intervals ranging from 10 to 90 minutes were tried in preliminary short Markov Chains, and the maximal values for  $\beta_r$ , 1.12, was used in our analysis.

We performed two new MCMC analysis, one with a transit of 55 Cnc e, and one without. Fig. 4 shows the resulting best-fit transit model and its residuals. The Bayes factor (Eq. 2 alone) *vs* (Eq. 2 + transit) is  $\sim 10^8$  in favor of the transit model. The transit of 55 Cnc e is thus firmly detected. Table 2 presents the resulting transit and physical parameters and  $1\sigma$  error limits derived for 55 Cnc e.

To test the robustness of our transit detection and of the resulting transit parameters, we performed  $\sim 10$  more MCMC analysis as described above, each of them assuming a different model for the systematic effects, e.g. without the sinus term in Eq. 2, without the terms in  $\log dt$ , with a different time polynomial, without it, etc. While none of these models revealed to be better than our nominal model for representing our *Warm Spitzer* data (Bayes factor between  $10^3$  and  $10^{15}$ ), each of these models lead to a decisive detection of the transit of 55 Cnc e (Bayes factor between  $10^{10}$  and  $10^{50}$ ). For all these alternatives models, the deduced values for the transit parameters agreed well with the ones deduced in our nominal analysis, except for the transit depth obtained without the two last terms of Eq. 2,  $650 \pm 80$  ppm. Nevertheless, our Bayesian comparison of both models makes this alternative model  $> 10^8$  times less probable than our nominal. We thus not only conclude to our firm detection of a transit of 55 Cnc e, but also to the robustness of the deduced results shown in Table 2.

$(R_p/R_*)^2$ [ppm]	$450 \pm 50$
$b = a \cos i / R_*$ [ $R_*$ ]	$0.16^{+0.10}_{-0.09}$
Transit width $W$ [d]	$0.0684^{+0.0010}_{-0.0009}$
$T_0 - 2450000$ [BJD]	$5568.0260^{+0.0012}_{-0.0006}$
$R_p/R_*$	$0.0213^{+0.0011}_{-0.0012}$
$a/R_*$	$3.442^{+0.068}_{-0.092}$
$R_*$	$0.97 \pm 0.02$
Inclination $i$ [deg]	$83.4^{+1.5}_{-1.7}$
Radius $R_p$ [ $R_\oplus$ ]	$2.13^{+0.14}_{-0.13}$

**Table 2.** Median and  $1\sigma$  limits of the posterior distributions derived for 55 Cnc e from our global MCMC analysis.

## 4. Discussion and conclusions

### 4.1. Photometric precision of *Warm Spitzer*

Because we have to take into account three different instrumental effects in addition to a possible smooth variation of the stellar flux, the complexity of our photometric baseline model is large (13 free parameters, Eq. 2). This illustrates well the challenge of ultra-precise time-series IR photometry, especially with a detector that is no longer actively cooled. By modeling this baseline in addition to the transit in our MCMC analysis, we naturally take into account its uncertainties and their impact on the deduced transit parameters. Despite the complexity of the baseline model, we reach a very good precision on these transit parameters. This is due not only to the extensive characterization of the *Warm Spitzer* instrumental effects performed by the exoplanet community and the *Spitzer* Science Center, but also by the extremely high-cadence made possible by the IRAC subarray mode. Indeed, we have here more than 5,000 photometric measurements to constrain thoroughly the 13+4 parameters of our global model. We show here that *Warm Spitzer* can not only detect an eclipse of a few hundreds of ppm, it can also measure its depth with a precision of  $\sim 50$  ppm, leading to the conclusion that this space telescope has still an important role to play for the detection and characterization of transiting planets.

### 4.2. Planetary radius

Our MCMC results (see Table 2) yield a planetary radius of  $2.13^{+0.14}_{-0.13} R_\oplus$  as measured in IRAC 4.5  $\mu\text{m}$  channel. This value is  $\sim 3\sigma$  larger than the radius of  $1.63 \pm 0.16 R_\oplus$  as determined in the visible by Winn et al. (2011).

The main reason for this discrepancy is that our transit depth of  $450 \pm 50$  ppm is 2.5 times larger than the one observed by *MOST*.

A secondary reason (at the  $\sim 10\%$  level) is the stellar radius value. As part of this work, we used the V magnitude, parallax and spectroscopic  $T_{\text{eff}}$  (Valenti & Fischer 2005) to derive a stellar radius of  $0.95 \pm 0.02 R_\odot$ , instead of employing the interferometric-derived value of  $1.1 \pm 0.1 R_\odot$  (van Belle & von Braun 2009) which yields a significantly lower stellar effective temperature. While this choice was motivated by the extensive spectroscopic coverage of 55 Cnc, we anticipate that additional observations will be motivated by the transiting nature of 55 Cnc e to pinpoint this value.

### 4.3. Composition of 55 Cnc e

To investigate the composition of 55 Cnc e we first consider the possibility that the visible and infrared wavelengths are measuring different planetary “surfaces” — the visible wavelength measuring the actual surface and the infrared wavelength measuring an extended atmosphere. An exosphere of CO or CO<sub>2</sub> would provide a possible explanation for the planetary radius discrepancy described in Sect. 4.2. These molecules are indeed strongly absorbing at 4.5  $\mu$ m, but not in the visible. The idea of CO to explain increased planetary emission in *Spitzer*’s 4.5  $\mu$ m channel has been considered before for WASP-12 (Li et al. 2010) and for CoRoT-2b (Deming et al. 2011). A thorough discussion of this possibility is however beyond the scope of the current paper.

The second possibility we consider is to interpret the 4.5  $\mu$ m radius at face value to investigate the composition of 55 Cnc e. We used the internal structure model described in Valencia et al. (2010) suitable for rocky and gaseous planets. We considered four different rocky compositions that span the possible range in radius. The upper bound for the radius is set by the lightest rocky composition, which is one where there is no iron. A planet with a radius larger than this upper limit, necessarily has volatiles. The lower bound for the radius is set by a pure iron composition. Both extreme compositions are unlikely to exist given that iron, magnesium and silicate have similar condensation temperatures, with the latter two making up most of the mantle of the Earth (i.e. Mg<sub>0.9</sub>Fe<sub>0.1</sub>O + SiO<sub>2</sub>). The other two rocky compositions are an Earth-like one (33% iron core, 67% silicate mantle with 0.1 of iron by mol) and a “super-Mercury” (63% iron core, 37% silicate mantle no iron). We also consider volatile compositions in which we added different amounts of H<sub>2</sub>O or hydrogen and helium (H-He) at an equilibrium temperature of  $\sim 2000$  K above an earth-like nucleus.

The radius obtained in our study  $2.13^{+0.14}_{-0.13} R_{\oplus}$  is larger than the upper limit of a rocky planet, requiring that 55 Cnc e have volatiles in its composition. We find that an envelope of 0.1% of H-He or  $\sim 20\%$  water above an Earth-like core can fit the data well. In Fig. 5 we show the mass-radius relationships for the different compositions considered and the different known transiting super-Earths. Based on the same arguments proposed by Valencia et al. (2010) for CoRoT-7b, the timescale for evaporation of a H-He envelope would be too short ( $\sim$  a few My) for it to be considered as a plausible composition, whereas the timescale for water evaporation is of the same order of magnitude than that of the age of the system ( $\sim$  a few billion years). Thus, according to the *Spitzer* data analysed in this study, we favor a composition of an envelope of supercritical water above a solid, perhaps earth-like, nucleus. The exact amount of volatiles will depend on the composition of the solid nucleus, with a reasonable estimate around  $\sim 20\%$ .

Figure 6 shows the density as a function of mass of several transiting super-Earths. The *Spitzer* 4.5  $\mu$ m transit radius for 55 Cnc e leads to a very different interpretation of the planet composition (one requiring volatiles) than the *MOST* (Winn et al. 2011) planet composition (a compact planet likely without volatiles). We emphasize that a  $3\sigma$  discrepancy on the radius value leads to a very different composition, motivating further observational and theoretical studies on this interesting object. Indeed, further ob-

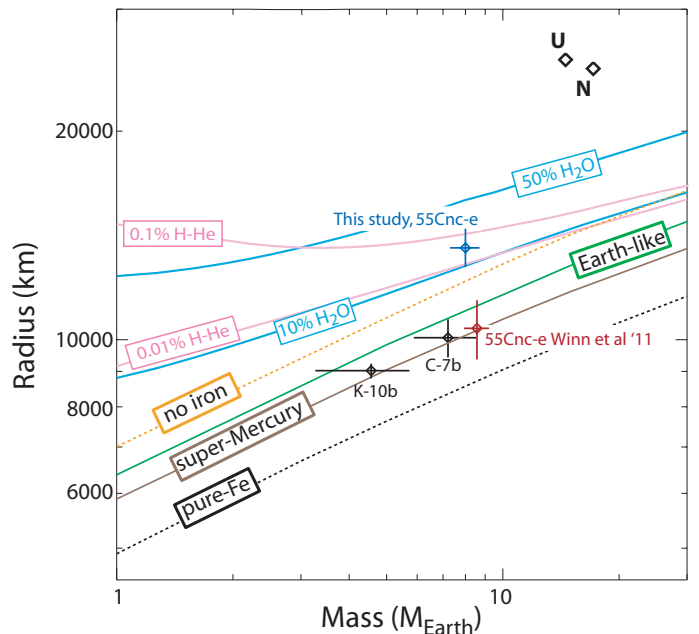


**Fig. 5.** Mass-Radius relationship for 55 Cnc e. We show four different rocky compositions: no iron, Earth-like (33% iron core, 67% silicate mantle with 0.1 of iron by mol), super-Mercury (63% iron core, 37% silicate mantle no iron), and a pure iron planet. We consider two types of volatiles compositions: 0.1-0.01% of H-He (pink), and 10-50% of water (blue) above an Earth-like nucleus. We show our data for 55 Cnc e (blue cross), that reported by Winn et al. (2011) (red), and the data for the known transiting hot super-Earths, Kepler-10b (K-10b – data from Batalha et al. 2011), and CoRoT-7b (C-7b data from Bruntt et al. 2010, Hatzes et al. 2011). Uranus and Neptune are shown for reference.

servations at different infrared and visible wavelengths will help to understand whether or not the 4.5  $\mu$ m data measure an extended atmosphere or exosphere, or if the 4.5  $\mu$ m data measures the same planetary surface as the visible-wavelength.

**Acknowledgements.** This work is based in part on observations made with the *Spitzer Space Telescope*, which is operated by the Jet Propulsion Laboratory, California Institute of Technology under a contract with NASA. Support for this work was provided by NASA. We thank the *Spitzer* Science Center staff for efficient scheduling of our observations. B.-O. Demory acknowledges support from the Swiss National Science Foundation in the form of a postdoctoral fellowship. M. Gillon is FNRS Research Associate. This publication makes use of data products from the Two Micron All Sky Survey, which is a joint project of the University of Massachusetts and the Infrared Processing and Analysis Center/California Institute of Technology, funded by the National Aeronautics and Space Administration and the National Science Foundation.

### References

- Bakos G. Á., Torres G., Pál A., et al. 2010, *ApJ*, 710, 1724
- Ballard S., Charbonneau D., Deming D., et al., 2010, *PASP*, 122, 1341
- Barge P., Baglin A., Auvergne M., et al., 2008, *A&A*, 482, L17
- Batalha N. M., Borucki W. J., Bryson S. T., et al., 2011, *ApJ*, 729, 27
- Bean J. L., Miller-Rici Kempton E., Homeier D., 2010, *Nature*, 468, 669
- Borucki W. J., Koch D. G., Basri G., et al., 2010a, *Science*, 327, 977
- Borucki W. J., Koch D. G., Brown T. M., et al., 2010b, *ApJ*, 713, L126



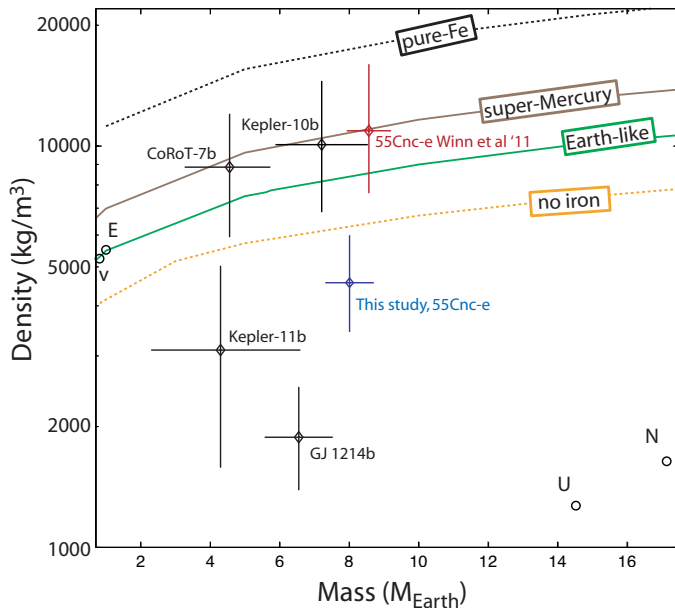


**Fig. 6.** Density vs mass of transiting super-Earths. The data for the known transiting super-Earths and mini-Neptunes is shown, as well as the relationships for the four rocky compositions considered in this study. Earth, Venus, Uranus and Neptune are shown for reference.

- Meschiari S., Wolf A. S., Rivera E., et al., 2009, *PASP*, 121, 1016  
 Naef D., Mayor M., Beuzit J. L., et al., 2004, *A&A*, 414, 351  
 Rafikov R. R., 2006, *ApJ*, 648, 666  
 Ricker G. R., Latham D. W., Vanderspek R. K., et al., 2010, *AAS Meeting 215, Bulletin of the American Astronomical Society*, 42, 459  
 Rogers L. A., Seager S., 2010, *ApJ*, 716, 1208  
 Seager S., Kuchner M., Hier-Majumder C. A., Militzer B., 2007, *ApJ*, 669, 1279  
 Seager S., 2010, *Exoplanet Atmospheres*, Princeton University Press  
 Shabram M., Fortney J. J., Greene T. P., Freedman R. S., 2011, *ApJ*, 727, 65  
 Skrutskie M. F., Cutri R. M., Stiening R., et al., 2006, *AJ*, 131, 1163  
 Stetson P. B., 1987, *PASP*, 99, 111  
 Sumi T., Bennett D. P., Bond I. A., et al., 2010, *ApJ*, 710, 1641  
 Torres G., 2007, *ApJ*, 671, L65  
 Turon C., Creze M., Egret D., et al., 1993, *Bull. Inf. Centre Donnees Stellaires*, 43, 5  
 van Belle G. T., von Braun K., 2009, *ApJ*, 694, 1085  
 Van Leeuwen F., 2007, *A&A*, 474, 653  
 Valencia, D., Ikoma, M., Guillot, T., & Nettelmann, N. 2010, *A&A*, 516, A20  
 Valenti J. A., Fischer D. A., *ApJS*, 159, 141  
 Winn J. N., Matthews J. M., Dawson R., et al., 2011, *ApJ Letters* (submitted), arXiv:1104.5230

- Borucki W. J., Koch D. G., Basri G., et al. 2011, *ApJ* (submitted), arXiv:1102.0541  
 Bruntt H., Deleuil M., Fridlund M., et al., 2010, *A&A*, 519, A51  
 Carlin B. P., Louis T. A., 2008, *Bayesian Methods for Data Analysis*, Third Edition (Chapman & Hall/CRC)  
 Carter J. A., Winn J. N., Holman M. J., et al., 2011, *ApJ* (accepted), arXiv:1012.0376  
 Catala C., Arentoft T., Fridlund M., et al., 2010, *Proceeding of the meeting Pathways Towards Habitable Planets*. Eds. Coudé du Foresto V., Gelino D. M., Ribas I. San Francisco. ASP, 260.  
 Charbonneau D., Berta Z. K., Irwin J., et al., 2009, *Nature*, 462, 891  
 Claret A., Bloemen S., 2011, *A&A*, 529, A75  
 Dawson R. I., Fabrycky D. C., 2010, *ApJ*, 722, 937  
 Deming, D., et al. 2011, *ApJ*, 726, 95  
 Désert, J. M., Lecavelier des Etangs A., Hébrard G., et al., 2009, *ApJ*, 699, 478  
 Désert, J. M., Bean J., Miller-Ricci Kempton E., et al., 2011, *ApJ*, 731, L40  
 Fazio G. G., Hora J. L., Allen L. E., et al., 2004, *ApJS*, 154, 10  
 Fischer D. A., Vogt S. S., Marcy G. W., et al., 2007, *ApJ*, 669, 1336  
 Fischer D. A., Marcy G. W., Butler R. P., et al., 2008, *ApJ*, 675, 790  
 Flower P. J., 1996, *ApJ*, 469, 355  
 Gillon M., Pont F., Demory B.-O., et al., 2007, *A&A*, 472, L13  
 Gillon M., Deming D., Demory B.-O., et al., 2010, *A&A*, 518, A25  
 Hartman J. D., Bakos G. Á., Kipping D. M., et al., 2010, *ApJ*, 728, 138  
 Hatzes A.P., Dvorak R., Wuchterl G., et al., 2010, *A&A*, 520, A93  
 Jeffreys H., 1961, *The Theory of Probability*, Oxford University Press  
 Knutson H.Á., Charbonneau D., Allen L.Á., et al., 2008, *ApJ*, 673, 526  
 Léger A., Rouan D., Schneider J., et al., 2009, *A&A*, 506, L287  
 Li, S.-L., Miller, N., Lin, D. N. C., & Fortney, J. J. 2010, *Nature*, 463, 1054  
 Lissauer J. J., Fabrycky D. C., Ford E. B., et al., 2011, *Nature*, 470, 53  
 Lovis C., Mayor M., Bouchy F., et al., 2009, *Transiting Planets, Proceedings of the International Astronomical Union, IAU Symposium 253*, 502  
 Mandel K., Agol E., 2002, *ApJ*, 580, 171  
 Mayor M., Udry S., Lovis C., et al., 2009, *A&A*, 493, 639  
 McArthur B. E., Endl M., Cochran W. D., et al., 2004, *ApJ*, 614, L81